Large Cu endowment in the Tibetan Plateau as a result of dual stage mantle fertilization

X. Wang, L. Gao, Z. Bai, M. Huang, J. Zhu, R. Yin

Supplementary Information

The Supplementary Information includes:

- Text S-1
- Tables S-1 to S-4
- Figures S-1 to S-5
- Supplementary Information References

Text S-1. Analytical Methods

Mercury isotope analyses were conducted using a Thermo Scientific Neptune Plus multi-collector inductively coupled plasma mass spectrometer (MC-ICP-MS) at the Institute of Geochemistry, Chinese Academy of Sciences. The instrument utilized a gas–liquid phase separator for introducing elemental Hg vapor and an Aridus for Tl aerosol generation. A 3 % (w/w) stannous chloride solution in 10 % (v/v) HCl was continuously mixed with Hg(II) solutions before being delivered into a frosted glass phase separator, where elemental Hg(0) vapor was generated via reduction. The generated Hg(0) vapor was subsequently blended with a dry aerosol of Tl produced by the Aridus prior to introduction into the plasma torch. A Jet sample cone and a nickel X-skimmer cone were employed to enhance sensitivity and signal stability. To correct instrumental mass bias during measurement, the NIST SRM 997 Tl standard ($^{205}Tl/^{203}Tl$ = 2.38714) was applied as an internal reference. The operating parameters during Hg isotope analysis were as follows: sample gas flow rate of 0.82–0.84 L/min, additional gas flow rate of 0.23–0.25 L/min, cooling gas flow rate of 16.0 L/min, auxiliary gas flow rate of 0.80 L/min, and radio frequency (RF) power of 1400 W. Sample uptake rates for Hg and Tl solutions in this study were about 0.65 and 0.05 mL/min, respectively. The Hg-preconcentrated solutions were diluted to 1 ng/mL with 10–20 % (v/v) of acid mixture (HNO_3/HCl = 2/1, v/v) before Hg isotopic analysis. Mass bias correction was carried out using the sample–standard bracketing (SSB) method, and to ensure high precision, Hg concentrations in both samples and standard solution were adjusted to match within ±10 %. See Yin *et al.* (2016) for detailed methods.

Supplementary Tables

Table S-1 Hg concentrations and Hg isotopic compositions of sulfides collected from porphyry Cu belts of Tibetan Plateau.

Sample ID	Type	THg (ng/g)	δ^{199}Hg (‰)	δ^{200}Hg (‰)	δ^{201}Hg (‰)	δ^{202}Hg (‰)	Δ^{199}Hg (‰)	Δ^{200}Hg (‰)	Δ^{201}Hg (‰)	Latitude (N)	Longitude (E)	Altitude (m)	Depth(m)
Qulong deposit													
WQL21-1	Pyrite	5.40	-0.58	-1.15	-1.65	-2.14	-0.04	-0.07	-0.04	29°37'33"	91°35'18"	5307	–
QL21-4	Chalcopyrite	211	-0.20	-0.39	-0.65	-0.79	0.00	0.01	-0.06	29°37'33"	91°35'18"	5307	–
QL21-6-1	Chalcopyrite	31.8	-0.11	-0.20	-0.28	-0.29	-0.03	-0.05	-0.06	29°37'34"	91°35'29"	5292	–
QL21-6-2	Pyrite	8.44	-0.60	-1.10	-1.56	-1.93	-0.12	-0.13	-0.11	29°37'34"	91°35'29"	5292	–
QL21-7-1	Chalcopyrite	63.3	-0.34	-0.40	-0.68	-0.76	-0.15	-0.02	-0.11	29°37'34"	91°35'29"	5292	–
QL21-7-2	Pyrite	18.4	-0.37	-0.81	-1.18	-1.60	0.04	0.00	0.02	29°37'34"	91°35'29"	5292	–
QL21-9	Pyrite	2253	-0.05	-0.17	-0.24	-0.35	0.03	0.00	0.02	29°37'47"	91°35'36"	5310	–
QL21-20	Pyrite	11.5	-0.42	-0.66	-0.92	-1.31	-0.09	0.00	0.06	29°37'14"	91°36'27"	5276	–
QL21-21	Pyrite	11.1	-0.66	-1.11	-1.67	-2.10	-0.13	-0.06	-0.08	29°37'14"	91°36'27"	5276	–
ZK103-1	Pyrite	21.7	-0.59	-1.03	-1.61	-1.89	-0.11	-0.08	-0.19	–	–	–	204 m depth in ZK103
ZK1806-1	Pyrite	43.6	-0.35	-0.57	-0.94	-1.14	-0.06	0.00	-0.08	–	–	–	130.3 m depth in ZK1806
ZK1806-2	Pyrite	556	-0.19	-0.45	-0.66	-0.88	0.03	-0.01	0.00	–	–	–	142.9 m depth in ZK1806
ZK1806-5	Chalcopyrite	23.7	0.21	0.21	0.48	0.46	0.10	-0.02	0.14	–	–	–	221 m depth in ZK1806
ZK1806-11	Chalcopyrite	66.5	0.18	0.37	0.44	0.55	0.04	0.09	0.03	–	–	–	266 m depth in ZK1806
Zhibula deposit													
ZBL21-1	Chalcopyrite	11.6	-0.16	-0.35	-0.53	-0.70	0.02	-0.01	-0.01	29°35'51"	91°36'07"	5275	–
ZBL21-2	Chalcopyrite	29.3	-0.12	-0.27	-0.45	-0.57	0.03	0.01	-0.02	29°35'51"	91°36'07"	5275	–
ZBL21-3	Chalcopyrite	42.2	-0.09	-0.22	-0.39	-0.49	0.03	0.03	-0.02	29°35'51"	91°36'07"	5275	–
ZBL21-4-1	Chalcopyrite	13.6	-0.13	-0.29	-0.47	-0.59	0.02	0.01	-0.03	29°35'51"	91°36'07"	5275	–
ZBL21-4-2	Bornite	32.6	-0.12	-0.33	-0.51	-0.81	0.09	0.08	0.10	29°35'51"	91°36'07"	5275	–
ZBL21-5	Chalcopyrite	50.3	-0.06	-0.01	-0.05	-0.04	-0.05	0.01	-0.02	29°35'51"	91°36'07"	5275	–
ZBL21-7	Chalcopyrite	57.2	0.08	0.31	0.42	0.65	-0.09	-0.02	-0.07	29°35'51"	91°36'07"	5275	–
ZBL21-8	Chalcopyrite	24.6	-0.08	-0.07	-0.15	-0.14	-0.05	0.00	-0.04	29°35'52"	91°36'18"	5205	–

Table S-1 continued.

Sample ID	Type	THg (ng/g)	δ^{199}Hg (‰)	δ^{200}Hg (‰)	δ^{201}Hg (‰)	δ^{202}Hg (‰)	Δ^{199}Hg (‰)	Δ^{200}Hg (‰)	Δ^{201}Hg (‰)	Latitude (N)	Longitude (E)	Altitude (m)	Depth (m)
Jiama deposit													
KZK-2	Pyrite	328	0.10	0.19	0.28	0.31	0.02	0.04	0.04	–	–	–	52.4 m depth in 4300KZK-24
ZJJ-1	Bornite	437	0.15	0.37	0.54	0.69	-0.03	0.03	0.02	29°41'42"	91°45'03"	4676	–
ZJJ-2	Chalcopyrite	52.7	-0.09	-0.20	-0.29	-0.34	0.00	-0.03	-0.03	29°41'42"	91°45'03"	4676	–
ZJJ-3	Chalcopyrite	35.2	0.10	-0.07	0.07	-0.02	0.10	-0.06	0.08	29°41'42"	91°45'03"	4676	–
JM21-1-1	Chalcopyrite	86.5	-0.16	-0.31	-0.53	-0.57	-0.02	-0.02	-0.10	29°41'42"	91°45'03"	4676	–
JM21-1-2	Bornite	93.3	-0.12	-0.35	-0.63	-0.73	0.06	0.02	-0.09	29°41'42"	91°45'03"	4676	–
JM21-2	Bornite	739	-0.45	-0.77	-1.28	-1.43	-0.09	-0.05	-0.20	29°41'42"	91°45'03"	4676	–
JM21-6-2	Chalcopyrite	169	-0.23	-0.42	-0.62	-0.73	-0.05	-0.05	-0.07	29°41'42"	91°45'03"	4676	–
Yulong deposit													
YL924	Pyrite	4.69	-0.48	-0.85	-1.36	-1.76	-0.03	0.04	-0.03	–	–	–	287-294 m depth in ZK0812
YL-925-1	Pyrite	7.25	-0.09	-0.59	-0.83	-1.20	0.21	0.01	0.07	–	–	–	299-306 m depth in ZK0812
YL-925-2	Pyrite	5.02	-0.06	-0.45	-0.57	-0.91	0.17	0.01	0.11	–	–	–	299-306 m depth in ZK0812
YL1550-2	Pyrite	8.99	-0.88	-1.25	-1.90	-2.32	-0.29	-0.08	-0.15	31°24'36"	97°46'12"	4634	–
YL1552-2	Pyrite	1.90	-0.27	-0.52	-0.61	-0.97	-0.02	-0.03	0.12	31°24'36"	97°46'12"	4634	–
YL1525-7	Pyrite	0.77	-0.26	-0.70	-0.99	-1.42	0.09	0.01	0.08	31°24'36"	97°46'12"	4634	–
ZK0812-5	Pyrite	19.84	-0.34	-0.54	-0.82	-1.01	-0.09	-0.03	-0.06	–	–	–	260 m depth in ZK0812
ZK0812-6	Pyrite	1.58	-0.11	-0.30	-0.40	-0.43	0.00	-0.08	-0.07	–	–	–	300 m depth in ZK0812
ZK0812-7	Pyrite	4.11	-0.34	-0.60	-0.86	-1.15	-0.05	-0.02	0.01	–	–	–	330 m depth in ZK0812
ZK0812-10	Pyrite	31.18	-0.05	0.04	0.03	0.10	-0.07	-0.02	-0.05	–	–	–	465 m depth in ZK0812
ZK0812-11	Pyrite	8.00	-0.08	-0.03	-0.11	-0.14	-0.04	0.04	-0.01	–	–	–	490 m depth in ZK0812
ZK1007-39	Pyrite	4.29	0.09	0.37	0.46	0.85	-0.13	-0.06	-0.18	–	–	–	372 m depth in ZK1007
ZK1007-40	Pyrite	2.88	0.25	0.38	0.52	0.68	0.08	0.04	0.00	–	–	–	380 m depth in ZK1007
ZK1007-41	Pyrite	2.16	-0.15	-0.30	-0.41	-0.54	-0.01	-0.03	-0.01	–	–	–	385 m depth in ZK1007
ZK1007-44	Pyrite	6.69	-0.66	-0.89	-1.45	-1.58	-0.26	-0.09	-0.26	–	–	–	408 m depth in ZK1007
ZK1007-55	Pyrite	10.93	-0.94	-1.37	-2.29	-2.59	-0.29	-0.07	-0.34	–	–	–	500 m depth in ZK1007

Table S-2 Hg concentrations and isotopic composition of juvenile lower crust rocks and potassic-ultrapotassic rocks in the Tibetan Plateau.

Sample ID	Type	THg (ng/g)	δ^{199}Hg (‰)	δ^{200}Hg (‰)	δ^{201}Hg (‰)	δ^{202}Hg (‰)	Δ^{199}Hg (‰)	Δ^{200}Hg (‰)	Δ^{201}Hg (‰)	Latitude (N)	Longitude (E)
21ML-02	Juvenile lower crust rocks	0.12	0.03	0.06	0.11	0.19	-0.01	-0.03	-0.03	29°12'48"	94°04'26"
21ML-09		1.37	-0.18	-0.21	-0.37	-0.33	-0.10	-0.04	-0.12	29°12'50"	94°04'50"
21ML-13		0.17	-0.16	-0.23	-0.28	-0.15	-0.12	-0.16	-0.17	29°12'50"	94°04'50"
21ML-14		0.99	0.04	0.35	0.34	0.56	-0.10	0.07	-0.07	29°12'50"	94°04'50"
21ML-17		0.60	-0.06	0.06	0.07	0.30	-0.13	-0.09	-0.16	29°12'50"	94°04'50"
21ML-20		1.38	0.25	0.74	1.06	1.59	-0.15	-0.06	-0.13	29°13'57"	94°04'39"
21ML-21		0.26	-0.03	0.05	-0.04	-0.09	-0.01	0.09	0.03	29°13'57"	94°04'39"
21ML-22		0.75	-0.08	-0.08	-0.12	-0.11	-0.05	-0.03	-0.04	29°13'57"	94°04'39"
21ML-23		0.38	-0.03	0.17	0.10	0.20	-0.08	0.06	-0.05	29°13'57"	94°04'39"
21ML-24		0.61	-0.07	0.09	0.00	0.18	-0.12	0.00	-0.13	29°13'57"	94°04'39"
21ML-25		0.41	0.04	0.38	0.32	0.63	-0.11	0.07	-0.15	29°13'57"	94°04'39"
21ML-26		0.67	-0.12	0.15	0.13	0.17	-0.16	0.07	0.00	29°13'57"	94°04'39"
21ML-27		0.35	-0.03	0.10	0.06	0.34	-0.11	-0.07	-0.20	29°13'57"	94°04'39"
21ML-28		2.67	0.01	0.22	0.13	0.48	-0.11	-0.02	-0.23	29°13'57"	94°04'39"
21ML-29		1.62	-0.08	0.08	-0.04	0.23	-0.14	-0.04	-0.22	29°13'57"	94°04'39"
21ML-30		0.50	-0.14	0.05	-0.17	0.09	-0.16	0.00	-0.24	29°13'57"	94°04'39"
21ML-31		1.16	0.00	0.07	0.03	0.07	-0.02	0.04	-0.03	29°13'57"	94°04'39"
21ML-33		0.84	-0.05	0.24	0.30	0.61	-0.20	-0.07	-0.16	29°13'57"	94°04'39"
21ML-34		0.52	0.05	0.16	0.05	0.15	0.01	0.08	-0.06	29°13'57"	94°04'39"
DJC-21-01	Potassic-ultrapotassic magmatic rocks	0.29	-0.44	-0.78	-1.16	-1.48	-0.07	-0.04	-0.05	29°46'54"	85°45'31"
JC-21-02		0.69	-0.23	-0.57	-0.81	-1.16	0.06	0.01	0.06	29°07'44"	94°00'26"
KDC-21-05		1.26	-0.32	-0.44	-0.60	-0.68	-0.15	-0.09	-0.08	30°56'32"	86°23'31"
YY-21-02		0.67	-0.17	-0.31	-0.42	-0.57	-0.03	-0.02	0.01	29°43'19"	94°22'19"
YJB-21-02		6.03	-0.55	-0.35	-0.72	-0.48	-0.42	-0.11	-0.36	29°55'55"	90°20'24"

Table S-3 Whole-rock major (wt. %) compositions of the juvenile lower crust rocks and potassic-ultrapotassic magmatic rocks of Tibet Plateau.

Sample ID	Type	SiO_2	TiO_2	Al_2O_3	Fe_2O_3	MnO	MgO	CaO	Na_2O	K_2O	P_2O_5	LOI	Total
21ML-02	Juvenile lower crust rocks (Sun *et al.*, 2024)	45.1	0.32	4.25	13.3	0.20	26.2	7.62	0.70	0.17	0.02	2.19	100
21ML-09		41.3	1.83	18.4	15.2	0.12	6.81	11.6	2.24	0.39	0.03	1.40	99.4
21ML-13		41.1	1.85	19.1	15.4	0.11	7.07	11.4	2.15	0.51	0.03	1.95	101
21ML-14		41.4	1.85	18.3	15.0	0.13	7.25	11.2	2.15	0.52	0.05	1.77	99.6
21ML-17		41.6	2.16	16.6	15.8	0.12	7.89	11.3	1.96	0.58	0.04	1.83	100.0
21ML-20		44.1	1.54	10.9	11.5	0.16	14.8	10.6	1.60	1.33	0.02	2.72	99.2
21ML-21		44.7	1.60	11.1	10.6	0.15	15.2	11.9	1.58	0.76	0.02	1.85	99.5
21ML-22		49.6	0.51	5.35	12.8	0.23	16.0	12.1	0.96	0.18	0.11	2.61	100
21ML-23		42.5	1.16	16.3	14.0	0.20	9.98	11.0	2.22	0.66	0.16	1.73	99.9
21ML-24		42.3	1.18	16.0	14.0	0.20	10.3	10.9	2.19	0.51	0.20	2.24	100
21ML-25		45.6	0.61	6.07	12.5	0.18	22.1	10.1	0.98	0.26	0.01	1.22	99.6
21ML-26		47.0	0.88	8.19	10.3	0.17	15.7	14.5	1.27	0.26	0.01	1.75	100
21ML-27		46.3	0.75	7.49	11.3	0.17	18.1	10.5	1.02	0.22	<0.01	3.02	98.8
21ML-28		42.5	1.92	13.6	12.6	0.16	14.0	10.4	2.02	1.22	0.01	1.86	100
21ML-29		43.5	1.54	12.6	11.1	0.14	14.8	11.2	1.95	0.88	0.02	2.33	99.9
21ML-30		43.7	1.40	11.7	11.2	0.16	14.8	11.2	1.70	1.32	0.06	2.7	99.9
21ML-31		47.6	0.90	7.67	10.7	0.19	16.5	12.7	1.34	0.25	0.01	1.73	99.6
21ML-33		46.7	0.98	8.56	11.1	0.21	17.2	10.8	1.40	0.42	0.01	2.37	99.7
21ML-34		48.2	0.61	6.70	10.6	0.19	16.8	12.9	1.00	0.21	0.04	2.43	99.5
DJC-21-01	Potassic-ultrapotassic rocks	67.1	0.44	14.9	3.41	0.13	0.88	2.16	3.35	5.52	0.13	1.10	99.1
JC-21-02		53.2	1.04	12.2	8.75	0.14	9.64	6.22	1.20	3.57	1.49	1.74	99.1
KDC-21-05		59.4	0.99	13.9	4.30	0.06	2.68	3.37	2.60	8.72	0.63	2.78	99.5
YY-21-02		59.9	0.79	15.2	5.24	0.08	2.38	4.19	3.96	5.53	0.65	1.50	99.4
YJB-21-02		76.2	0.13	13.0	1.01	0.10	0.21	0.18	3.90	3.33	0.03	1.23	99.3
GBW07105	Standard materials	44.25	2.37	13.67	13.40	0.18	7.72	8.86	3.40	2.29	0.95		
GBW07105 *		44.64	2.37	13.83	13.40	0.17	7.77	8.81	3.38	2.32	0.95		
GBW07104												4.39	
GBW07104 *												4.44	

* Standard value from China National Standard Materials Center

Table S-4 Hg isotopic composition of NIST-3177 and GSS-4.

Sample ID	Date source	*n*	δ^{202}Hg (‰)	2 s.d.	Δ^{199}Hg (‰)	2 s.d.	Δ^{200}Hg (‰)	2 s.d.	Δ^{201}Hg (‰)	2 s.d.
NIST-3177	This study	10	-0.53	0.06	-0.02	0.04	0.01	0.03	-0.02	0.06
GSS-4		8	-1.64	0.13	-0.41	0.06	-0.02	0.06	-0.37	0.06
NIST-3177	Blum and Berquist (2007)	25	-0.54	0.08	-0.01	0.05	0.00	0.05	-0.04	0.04
NIST-3177	Deng *et al.* (2021)	11	-0.50	0.10	-0.01	0.05	–	–	-0.02	0.07
GSS-4		3	-1.67	0.14	-0.34	0.08	–	–	-0.35	0.07
NIST-3177	Gao *et al.* (2024)	4	-0.53	0.10	0.01	0.05	0.02	0.05	0.04	0.06
GSS-4		4	-1.64	0.10	-0.47	0.03	-0.02	0.06	-0.40	0.05

Supplementary Figures

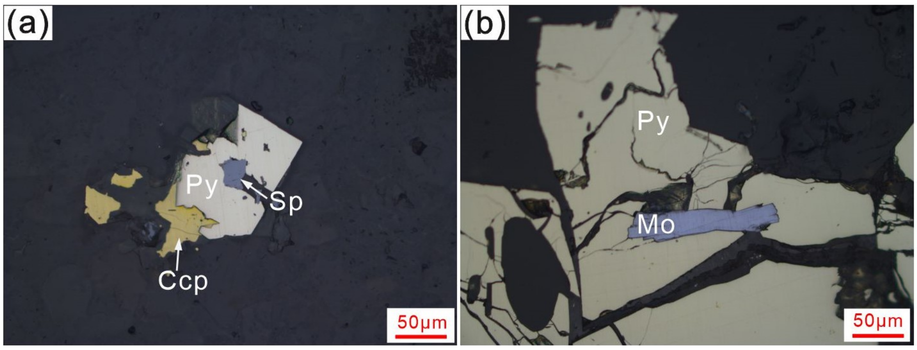

Figure S-1 Representative photomicrographs show the mineral assemblages of the Yulong porphyry Cu deposit. Py, pyrite; Ccp, chalcopyrite; Mo, molybdenite; Sp, sphalerite.

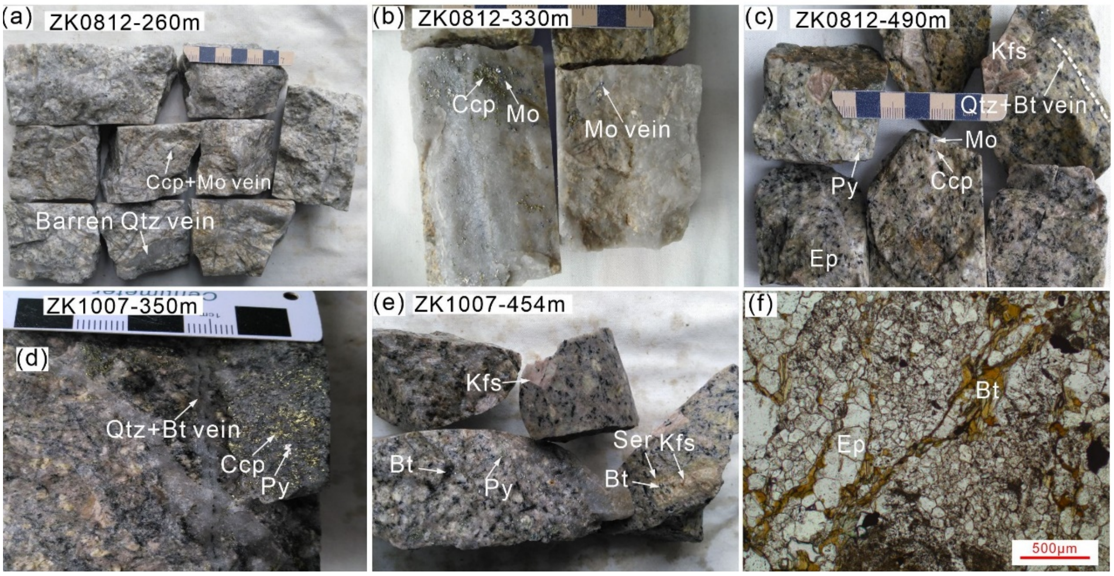

Figure S-2 **(a–e)** Photographs of hand specimens and **(f)** a typical microscopic image from the Yulong deposit. **(a)** Strongly silicified monzogranite porphyry, characterized by abundant quartz veinlets. **(b)** Chalcopyrite and molybdenite are distributed within the smoky quartz veins. **(c)** Potassic alteration is characterized by secondary biotite veins and disseminated secondary potassic feldspar. **(d)** Pyrite and chalcopyrite are disseminated within the quartz-biotite veins. **(e)** The hydrothermal K-feldspar coexists with hydrothermal biotite, and the borders are overprinted by sericitization. **(f)** Secondary biotite veins under the microscope. Ccp, chalcopyrite; Py, pyrite; Mo, molybdenite; Qtz, quartz; Bt, biotite; Ep, epidote; Ser, sericite; Kfs, K-feldspar.

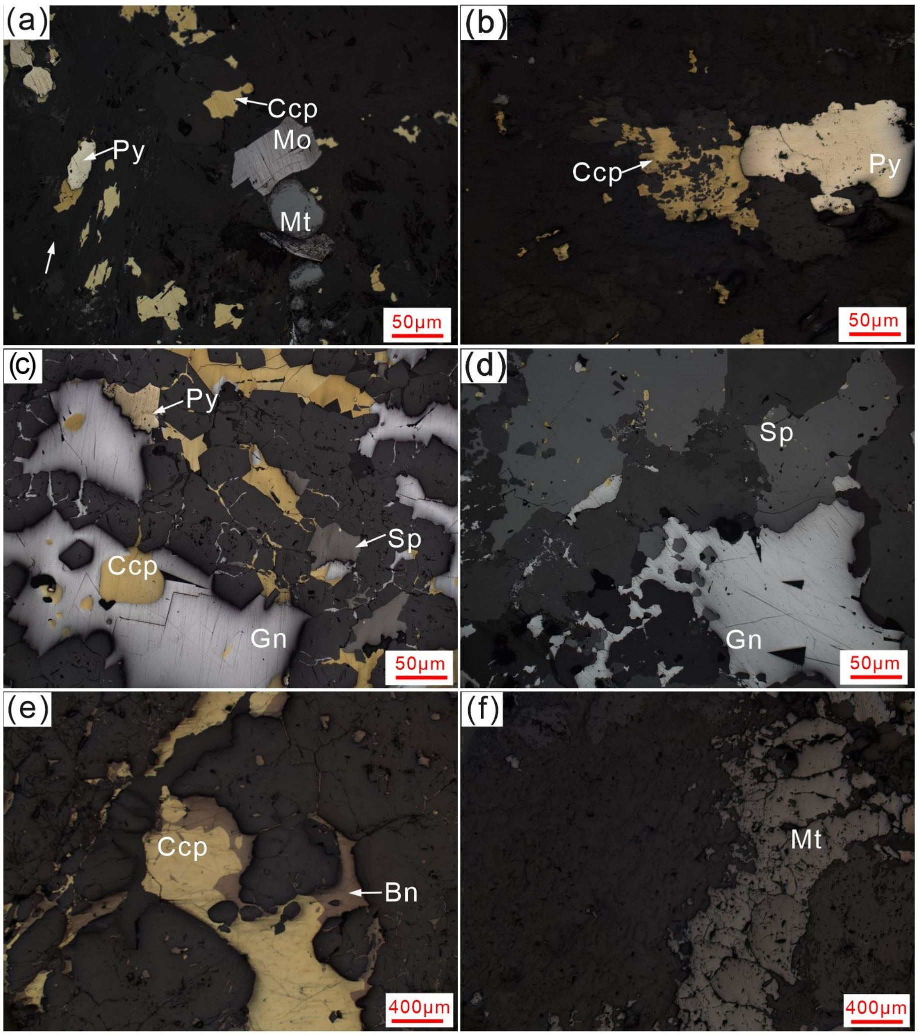

Figure S-3 Representative photomicrographs show the mineral assemblages of the Gangdese porphyry Cu deposits. Photomicrographs **(a, b)**, **(c, d)** and **(e, f)** represent the Qulong, Jiama and Zhibula deposits, respectively. Py, pyrite; Ccp, chalcopyrite; Mo, molybdenite; Mt, magnetite; Sp, sphalerite; Bn, bornite; Gn, galena.

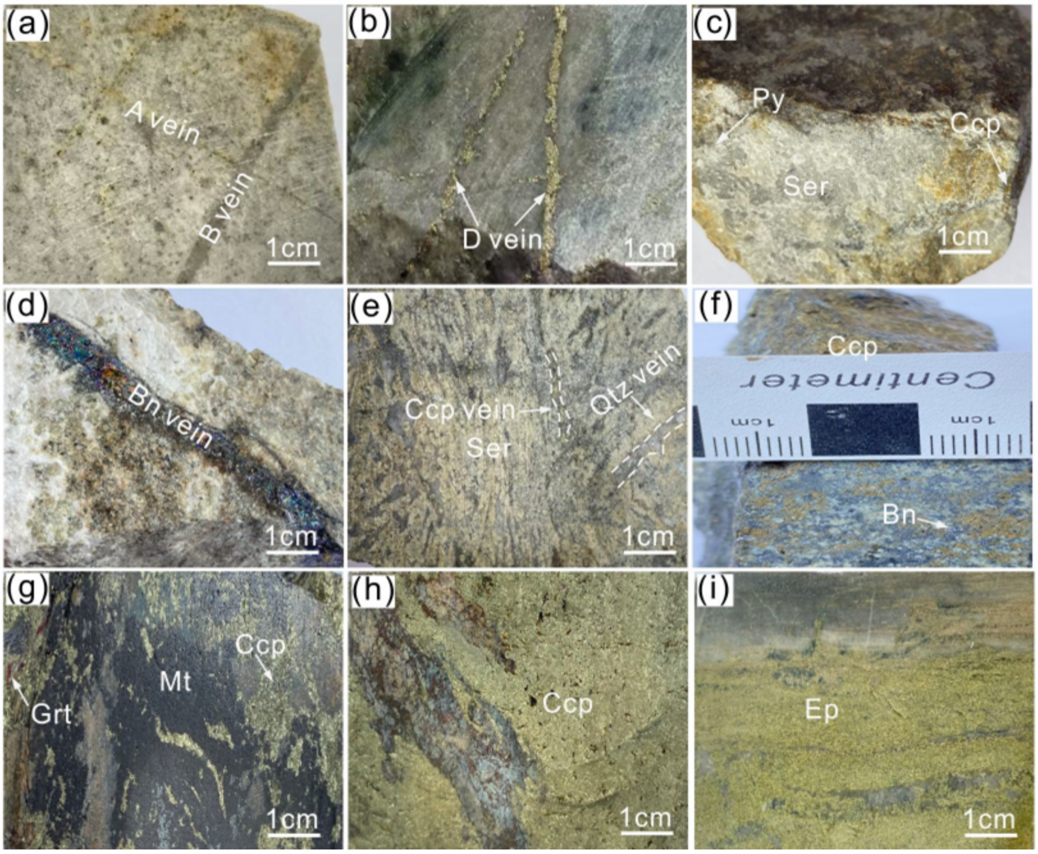

Figure S-4 Photographs of hand specimens from the Qulong, Jiama and Zhibula deposits. **(a–c)**, **(d–f)**, and **(g–i)** hand specimens from the Qulong, Jiama, and Zhibula deposits, respectively. **(a)** Quartz vein A is crosscut by the later-formed quartz vein B. **(b)** Late-stage D veins, primarily composed of pyrite, and characterized by typical pyrite-sericitic alteration. **(c)** Intense sericitic alteration, with disseminated pyrite and chalcopyrite. **(d)** A bornite vein cutting through skarn. **(e)** The hand specimen shows strong sericitic alternation, accompanied by fine quartz veins and chalcopyrite veins. **(f)** Chalcopyrite-bornite ore. **(g)** Skarn, primarily composed of garnet, magnetite, and bornite. **(h)** Massive chalcopyrite ore. **(i)** Large-scale epidotization alteration. Bn, bornite; Ccp, chalcopyrite; Ep, epidote; Grt, garnet; Mt, magnetite; Qtz, quartz; Ser, sericite.

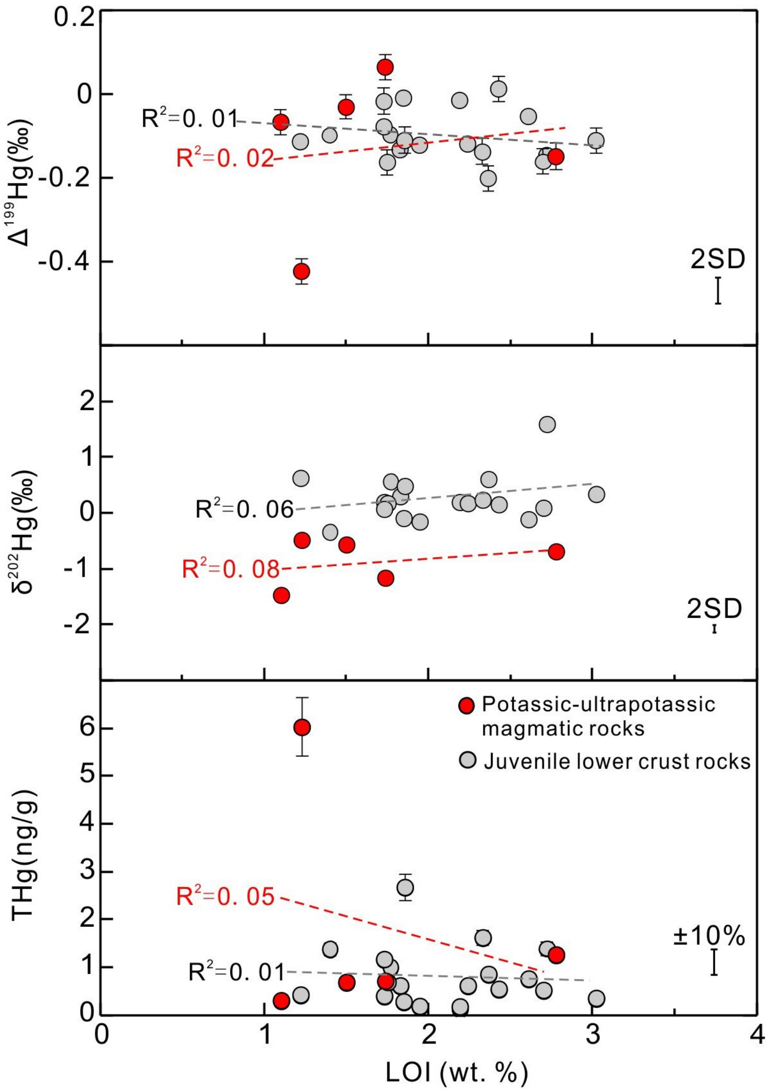

Figure S-5 Correlations between LOI values and Hg concentrations, δ^{202}Hg or Δ^{199}Hg values of juvenile lower crust rocks and potassic-ultrapotassic magmatic rocks in the Tibetan Plateau. The LOI data of the juvenile lower crust rocks in the Tibetan Plateau from Sun *et al*. (2024).

References

Blum, J.D., Bergquist, B.A. (2007) Reporting of variations in the natural isotopic composition of mercury. *Analytical and Bioanalytical Chemistry* 388, 353–359. https://doi.org/10.1007/s00216-007-1236-9

Deng, C., Sun, G., Rong, Y., Sun, R., Sun, D., Lehmann, B., Yin, R. (2021) Recycling of mercury from the atmosphere-ocean system into volcanic-arc–associated epithermal gold systems. *Geology* 49, 309–313. https://doi.org/10.1130/G48132.1

Gao, L., Sun, D., Wang, X., Chen, D., Tian, Z., Luo, A., Yin, R. (2024) A Catalyst Tube-Equipped Dual-Stage Tube Furnace System for Accurate Hg Isotopic Determination of Ore Samples Using Neptune Plus Multicollector Inductively Coupled Plasma Mass Spectrometry. *Analytical Chemistry* 96, 17560–17566. https://doi.org/10.1021/acs.analchem.4c03041

Sun, J.-L., Bai, Z.-J., Zhong, H., Liu, X., Zhu, J.-J., Chen, L., Zhu, W.-G. (2024) Sulfide saturation in reduced magmas during generation of the Gangdese juvenile lower crust: Implications for porphyry Cu–Au mineralization in the Gangdese belt, Tibet. *Mineralium Deposita* 59, 1387–1405. https://doi.org/10.1007/s00126-024-01269-0

Yin, R., Krabbenhoft, D.P., Bergquist, B.A., Zheng, W., Lepak, R.F., Hurley, J.P. (2016) Effects of mercury and thallium concentrations on high precision determination of mercury isotopic composition by Neptune Plus multiple collector inductively coupled plasma mass spectrometry. *Journal of Analytical Atomic Spectrometry* 31, 2060–2068. https://doi.org/10.1039/C6JA00107F.